J. Fluid Mech. (1985), *vol.* 159, *pp.* 503–531
Printed in Great Britain

Two-layer model of shear-driven coastal upwelling in the presence of bottom topography

By SIAVASH NARIMOUSA AND TONY MAXWORTHY
Department of Mechanical Engineering, University of Southern California,
Los Angeles, CA 90089-1453

(Received 2 January 1985 and in revised form 8 April 1985)

A stratified two-layer fluid is brought to solid-body counterclockwise rotation inside a cylindrical tank having a conical bottom with a radial topographic ridge. A stress is then applied to the top surface by means of a clockwise differentially rotating disk. The resulting Ekman-layer flux causes the top layer to spin-down and the interface to rise near the wall and to descend at the centre of the tank. As this process continues, the interface (front) between the two layers intersects the disk surface, and after that migrates away from the wall and allows the bottom fluid to contact the disk directly. The migration of the front continues until a steady state is reached, the front becomes stationary and the system is in geostrophic balance. The first sign of upwelled flow at the surface always occurs as a high-speed jet-like plume at the bottom topography, and only at a later time does a uniform upwelled flow appear at the surface upstream of the topography. This plume, which always forms near the downstream edge of the topography, migrates in advance of the upstream front to produce an upwelling maximum at the bottom topography.

The final width of the upstream flow in steady-state conditions is estimated by a simple theoretical model, which is in good agreement with the experimental results. We have an experimental criterion to predict the occurrence of travelling baroclinic waves on the upstream front. On the downstream side of the ridge, large standing waves are observed, with significant upwelling within them. Under some circumstances cyclones pinch-off from the upstream front, the plume on the ridge and the crests of the large downstream standing waves. We present criteria to predict the occurrence of these pinch-off processes.

1. Introduction

During the last two decades, extensive work has been done on the dynamics of coastal upwelling in coastal regions such as those off Oregon, California, West Africa and Peru. Each of these regions has its own special geography, i.e. shape of the coast and presence of bottom topography. In general, a favourable alongshore wind stress causes the surface layer to drift offshore and allows cold, nutrient-rich, bottom fluid to upwell and appear at the surface. For example, this phenomenon has been demonstrated by the field work of Halpern (1974, 1976) and Mooers, Collins & Smith (1976) off the coast of Oregon, and Brink, Halpern & Smith (1980) off Peru. Theories due to Allen (1973), Garvine (1971), and the numerical models of O'Brien & Hulburt (1972), Hulburt & Thompson (1973), Ikeda & Emery (1984) have clarified some of the dynamical features that have been observed.

It was thought for some time that the strongest upwelling should occur on the downstream side of capes (see Arthur 1965; Yoshida 1967). Peffley & O'Brien (1976)

studied the effects of variable coastline (capes) on upwelling, and their results indicate that coastline features have little effect on the dynamics of the longshore upwelling circulation. They concluded that the stronger upwelling, which may occur near the capes, is primarily due to local bottom topography and not to the capes themselves. As a result, Preller & O'Brien (1980) investigated the effects of local bottom topography on upwelling, and they found that an upwelling maximum, off Peru, is probably the result of interaction with a bottom topographic feature.

In the present work, we have been able to model coastal upwelling in the laboratory, and to examine the effects of bottom topography and capes on the upwelling front. In these experiments a stratified two-layer fluid system was brought to solid-body rotation in a cylindrical tank, and then a favourable stress was applied to the thin top surface. This produced an upwelling around the outer edge of the tank. In some experiments we placed a large bump (a cape) at the outer edge of the wall, and it was observed that this perturbation had only a minor effect on the upwelling process. This experimental result is consistent with the numerical models of Peffley & O'Brien (1976). In other preliminary experiments we placed topography on the sloping bottom of the cylindrical tank, and we noticed that it had a dramatic influence on the dynamics of the coastal upwelling. Because of this, the body of this paper focuses on a study of the effects of the bottom topography on coastal upwelling, while the study of the effect of a coastline protuberance is left to a separate paper.

The front upstream of the topography was observed to migrate outward, until a geostrophic balance was reached and the front becomes stationary. Usually, before the front became stationary, non-axisymmetric disturbances (baroclinic waves) occurred at the front. The stability of a front to such disturbances has already been discussed by Eady (1949), Hide (1971), Hart (1972, 1980), Douglas, Hide & Mason (1972), Saunders (1973) and Griffiths & Linden (1981), among others. Previously, the appearance of baroclinic instability has been thought to occur when the Rossby deformation radius, non-dimensionalized by an appropriate lengthscale, was less than order unity. In our study we find that, besides the dimensionless Rossby deformation radius, there is another parameter which also determines the occurrence of instability of the baroclinic waves. This parameter we denote by $\theta_* = g'h_0/u_* f\lambda_s$, where $g' = g\,\Delta\rho$ is the reduced gravity between the two layers, $\Delta\rho$ is the density difference between the two layers, h_0 is the initial depth of the lighter fluid, $f = 2\Omega$ is the Coriolis parameter, u_* is the disk friction velocity at the location of the upwelled front, and λ_s is the final distance of the upstream front from the wall. We also find that θ_*, which is a combination of the dimensionless Rossby radius $\theta = (g'h_0)^{\frac{1}{2}}/f\lambda_s$ and the Richardson number $Ri_* = g'h_0/u_*^2$, is a suitable parameter to characterize the dynamics of coastal upwelling, as well as the size and drift velocity of the baroclinic waves.

Upwelling close to the bottom topography is discussed in §6, and is compared with the numerical model of Preller & O'Brien (1980) and Ikeda & Emery (1984). The dynamics of the flow downstream of the topography is found to be very different from that upstream, as also shown in detail in §6.

2. The experiment

The experimental apparatus consists of a cylindrical tank 90 cm in diameter and 22 cm in depth, rigidly mounted on a rotating table (see figure 1). To study the effect of bottom topography on the upwelling front, a conical surface is placed symmetrically inside the tank, thus reducing the depth of the tank to 6 cm at the wall, and increasing linearly towards the centre of the tank with a slope $\alpha = 0.27$. A ridge, manufactured

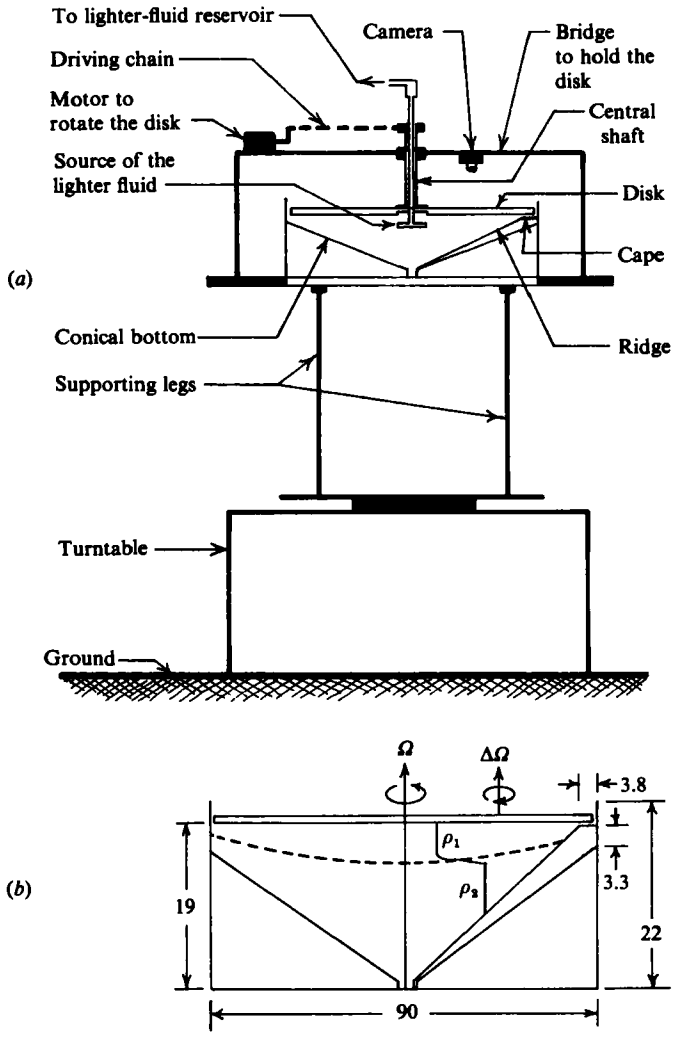

FIGURE 1. (*a*) Side view of the experimental apparatus. (*b*) Side view of the experimental tank, with a cross-section at the ridge (lengths measured in centimetres).

by cutting a cone in half, is placed on a suitable area of the conical bottom on its flat side. It has a maximum width W of 7.6 cm at the wall, gradually decreasing to zero at the centre of the tank. The maximum height of the ridge is 3.2 cm at the wall, and it is cut so as to extend 3.8 cm outward to produce a cape (see figure 1).

To model the wind stress, a circular smooth disk 2.3 cm thick is mounted on a central shaft in the upper part of the tank, so that the working depth of the tank is reduced to 3.3 cm at the wall, and gradually increases to 15.4 cm at the centre of the tank. A gap of about 1 mm is left between the disk and the top of the ridge to avoid any mechanical interaction between the two (see figure 1). In this way, the first 3.8 cm (i.e. the width of the cape) of the longshore flow is blocked. This disk can be set to rotate in either direction with respect to the rotating tank by means of a variable-speed motor and chain drive, as shown in figure 1.

To investigate the dynamics of local upwelling, the tank is filled with two superimposed layers of miscible homogeneous fluid of slightly different densities. This

two-layer system is generated in the following way. First the tank is filled to a required depth with the heavier salt solution. Then the turntable is set to rotate at a desired rotation rate and the fluid brought to a solid-body rotation. The lighter fluid (also a salt solution) is then allowed to flow radially on top of the denser rotating fluid by means of a diffuser, so as to avoid mixing, as shown in figure 1. Thus the lighter fluid, while flowing on top of the heavier fluid, is also brought to solid-body rotation. This process usually continues until the lighter fluid fills the tank. For the purpose of this study, the initial depth h_0 of the lighter fluid is chosen to be much smaller than the maximum depth of the denser fluid, and the disk is set to rotate in the direction opposite to the turntable rotation; this produces an upwelling front around the outer edge of the tank. A number of preliminary experiments were conducted to choose a suitable $\Delta\Omega$ (disk rotation rate) to avoid strong turbulent mixing at the upwelling front; this $\Delta\Omega$ (0.125 rad/s) was then kept the same for all the experiments reported in this paper.

To observe the upwelling front, small neutrally buoyant particles were placed in the interface between the two fluids and their motion observed by streak photography. The direction of motion of these particles was found by firing an electronic flash at the beginning of the $\frac{1}{2}$ s time exposure of a 35 mm Nikon camera, which was placed at a distance of 60 cm above the disk (see figure 1). These particles have an average density of about 1.035 g/cm^3. The two fluid densities ρ_1 and ρ_2 (ρ_1 is density of the lighter fluid and ρ_2 that of the heavier fluid) are chosen in such a way as always to keep the particles in the interface. For example, if $\Delta\rho = 0.03$ g/cm^3 then values of $\rho_1 = 1.02$ g/cm^3 and $\rho_2 = 1.05$ g/cm^3 are chosen, so that the density in the centre of the interface is about 1.035 g/cm^3. Eight experiments are reported in this paper, and the experimental parameters are as follows: $2.1 \leqslant h_0 \leqslant 2.6$ cm, $0.02 \leqslant \Delta\rho_0 \leqslant 0.024$ g/cm^3, $\Delta\Omega = 0.125$ rad/s, and the Coriolis parameter is in the range $1.244 \leqslant f \leqslant 5.8$ rad/s. The above-mentioned dimensions of the experimental apparatus, the disk, the conical bottom and the ridge are kept the same for all experiments.

3. A general description of the flow

When a stress was applied to the top surface of the unobstructed system by the differentially rotating disk, it began to spin-down the top layer, lowering the level of the interface at the centre of the tank and raising it near the wall. As this process continued, the interface intersected the surface at the outer edge of the wall, and after that the lighter fluid migrated away from the wall and allowed the bottom fluid to appear at the surface near the outer edge. We denote the distance of the front from the wall by λ, and this is identical with the width of the bottom fluid at the surface. We call the depth of the front from the surface at any given point $\eta(r)$. In this process the Coriolis force associated with the azimuthal velocity of the axisymmetric flow tends to increase λ, while the radial pressure gradient caused by the front deformation opposes the Coriolis force, and tends to stop the front. Finally, the two forces balance (geostrophic balance), and the front becomes stationary, so that λ and η reach their steady-state values (λ_s and η_s). Note that in all experiments reported in this paper, the choice of the initial parameters was such that the largest value of η_s was always well above the bottom of the tank and such that before the steady state was reached baroclinic waves appeared at the upwelling front.

Repeating this experiment in the presence of the ridge caused a dramatic change in appearance of the upwelling front. In order to discuss these changes the present

study divides the experimental results into two parts: the first part discusses the dynamics of the flow upstream of the ridge and the second part concerns the dynamics of the flow close to and downstream of the ridge. We consider that all the initial parameters are constant, and we only allow f to vary.

First we give a brief discussion of the upstream flow based on our observations. On figure 2 to the left of the obstacle we show sequences of photographs indicating migration of the front from the wall upstream of the ridge until the steady-state situation is reached. In a given experiment the speed of migration of the front u_f is constant, and approaches zero at steady state (see §6). During the upwelling process, before the steady-state situation was reached, non-asymmetric flow (baroclinic waves) appeared at the front (see figure 2*c*). These waves have a large azimuthal wave speed, with the larger wavelength waves drifting faster than the smaller ones (see §6). Larger waves were generated when the front was near the wall, while the smaller waves were generated when the front was far from the wall. This is due to the fact that for experiments with increased f the speed of migration of the front u_f increased, so that the waves did not have time to develop near the wall. Another feature of the waves is that, once they formed at the front, their size remained almost constant during the rest of the experiment, and their speed did not change. The frontal waves had the form of a train of dipolar cyclones and anticyclones (e.g. see figure 2*d*). Anticyclones were usually observed at the front closer to the wall, while cyclones were observed further from the wall, so that the wave crest was anticyclonic and the wave trough was cyclonic. The frontal cyclones, which were capable of carrying heavier fluid into the lighter fluid, often pinched-off from the front to form isolated vortices. For example, in the lower left corner of figure 3(*a*) a cyclone is about to be pinched off from the front. The pinched-off cyclones also had a large drift velocity, so that before they could travel too far from the front they reached the ridge and were distorted (see figure 3). This modification by the flow field around the ridge was true for both frontal cyclones and anticyclones.

The effect of the ridge on the upstream wave motion was to reduce considerably the speed of the waves (to about $\frac{1}{5}$ of the disk velocity), so that the structure of the cyclones and anticyclones could be observed clearly, as seen in figure 2(*d*). Without the ridge the speed of the waves was much larger (about $\frac{1}{2}$ of the disk velocity). This blocking effect of the ridge on upstream waves was stronger at higher rotation rates, so that the structure of the waves was more pronounced than at low rotation rates.

The presence of the ridge also gave rise to a meandering jet-like motion, starting from near the upstream edge of the ridge, and extending downstream to a distance almost equal to one radius of the tank. We believe that the shear in this jet is responsible for the disappearance of the upstream waves at the ridge, since it was observed that, as the upstream waves approached the ridge, they began to deform until they were incorporated into the jet and vanished as separate entities.

The first part of the jet was a plume containing heavier fluid; the head of the plume was always observed near the downstream edge of the ridge (e.g. see figure 2). The generation of the plume can be explained by simple vortex-stretching arguments in which the velocity induced by vortex contraction as fluid columns try to flow over the ridge is radially inward, reversing direction once past the ridge (Maxworthy 1979). This causes the front to deform and bulge away from the cape, to generate the abovementioned plume, which is also the first sign of upwelled flow at the surface in these experiments. During the course of any given experiment, the front on the ridge always migrated in advance of the upstream front and characterized an upwelling maximum. The migration velocity of the front on the ridge was approxi-

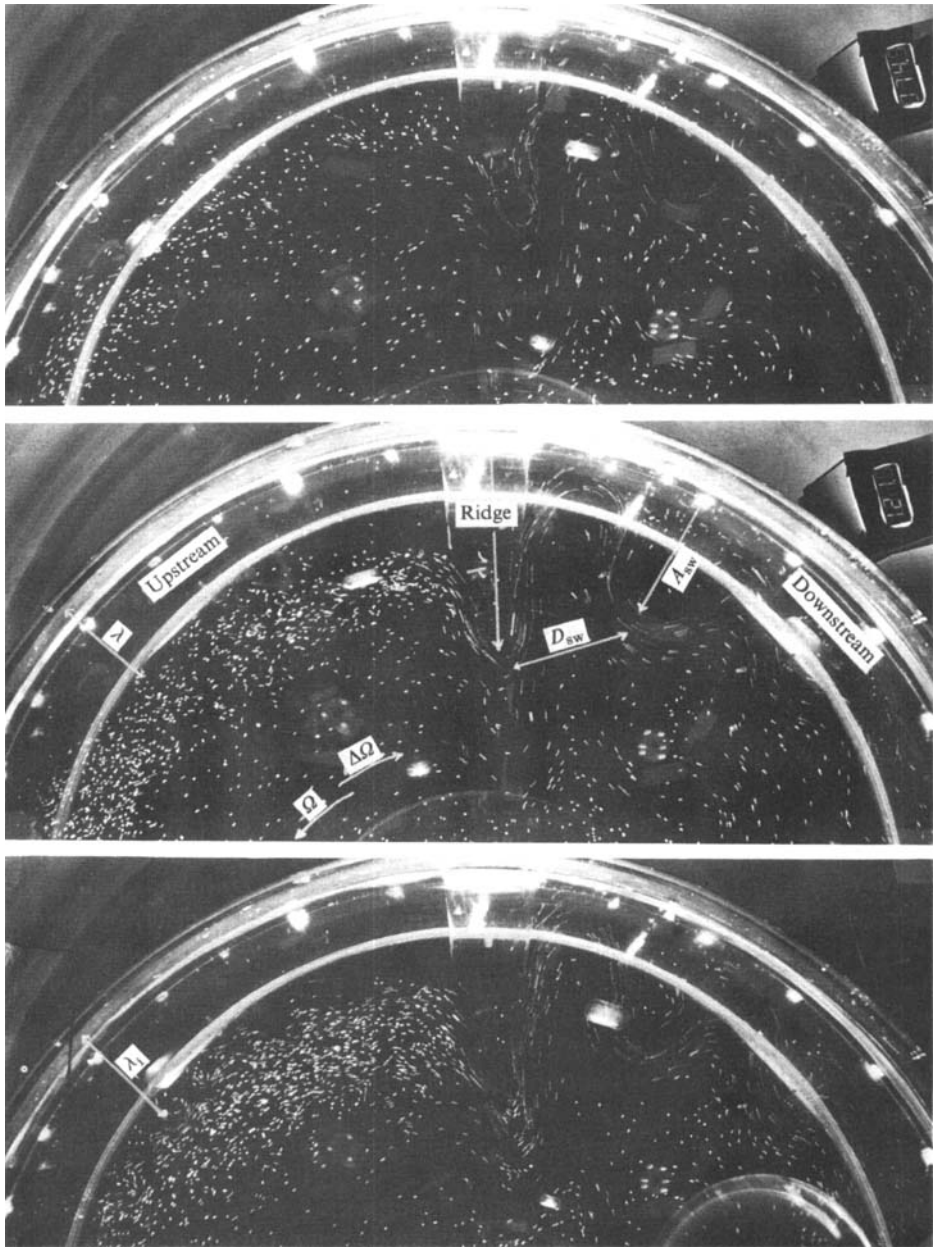

mately constant, since during migration the position of the maximum plume displacement vacillated.

A permanently trapped cyclone, containing heavier fluid, was always observed over or slightly downstream of the ridge, especially at lower values of f, under which circumstances the plume was more stable (see figure 5*c*). As f increased, the head of the plume became unstable and a cyclone containing bottom fluid was pinched-off and propagated into the lighter fluid (see figure 4). Usually this cyclone did not move

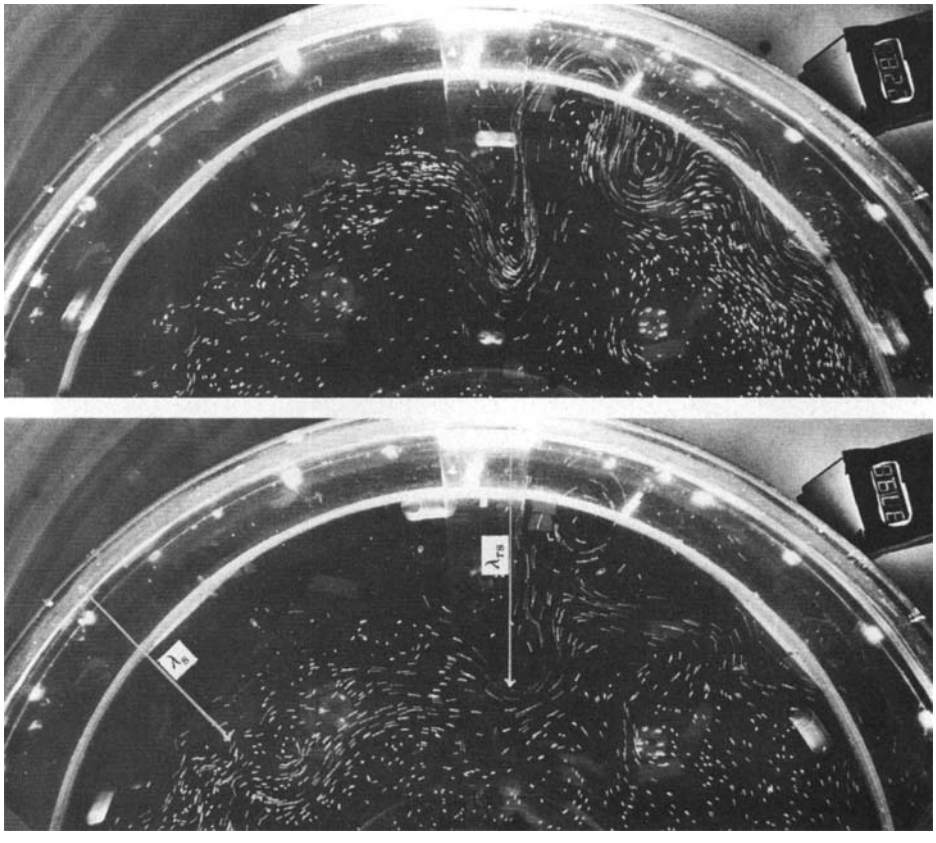

FIGURE 2. Photograph (*a*) was taken at $t = 74$ s. The upstream front (to the left of the ridge) has migrated about $\lambda = 5$ cm away from the wall, and the baroclinic waves have yet to appear at the upstream front. Notice the deformation of the front at the ridge (middle of (*a*)) in the form of a plume migrating outwards in advance of the upstream front. Also, large standing waves are formed downstream from the ridge (right-half side of (*a*)). Photograph (*b*) was taken at $t \simeq 121$ s, $\lambda \approx 7.5$ cm, showing that waves are still absent from the upstream (*b*). Photograph (*c*) was taken at $t \simeq 140$ s, $\lambda = \lambda_1 \approx 8$ cm. The first appearance of the baroclinic waves at the upstream front occurs at this time. Photograph (*d*), taken at $t \approx 228$ s, $\lambda_1 \approx 12.5$ cm, indicates that the upstream front and the front at the ridge are still migrating. Photograph (*e*), taken at $t \approx 373$ s, shows the steady-state stationary front with a value of $\lambda = \lambda_s \approx 16$ cm. In general, these photographs indicate (i) that the amplitude of the large downstream standing wave A_{sw} is almost a constant and the flow within it is cyclonic, (ii) maximum upwelling occurs at the ridge, and (iii) the appearance of the baroclinic waves at the upstream front does not occur immediately. The parameter values are $f = 4.6$ rad/s, $g' = 20.12$ cm/s^2, $h_0 = 2$ cm and $\Delta\Omega \approx 0.125$ rad/s. Certain measured quantities are also defined on figures 2(*b*, *c*, *e*).

too far from the plume; instead, it became incorporated into the jet after a few rotation periods and vanished as a separate entity. Note that this process often repeated itself during the course of a given experiment.

At higher values of f, near the downstream edge of the ridge, the direction of the jet was parallel to the ridge and radially outward all the way to the wall of the tank, where it was deflected by the wall to produce a large standing wave downstream of the plume maximum (see figure 2). Regardless of the development of the upstream front and maximum plume on the ridge, it took only about 10–15 rotation periods for the downstream standing wave to develop fully, and its amplitude was always close

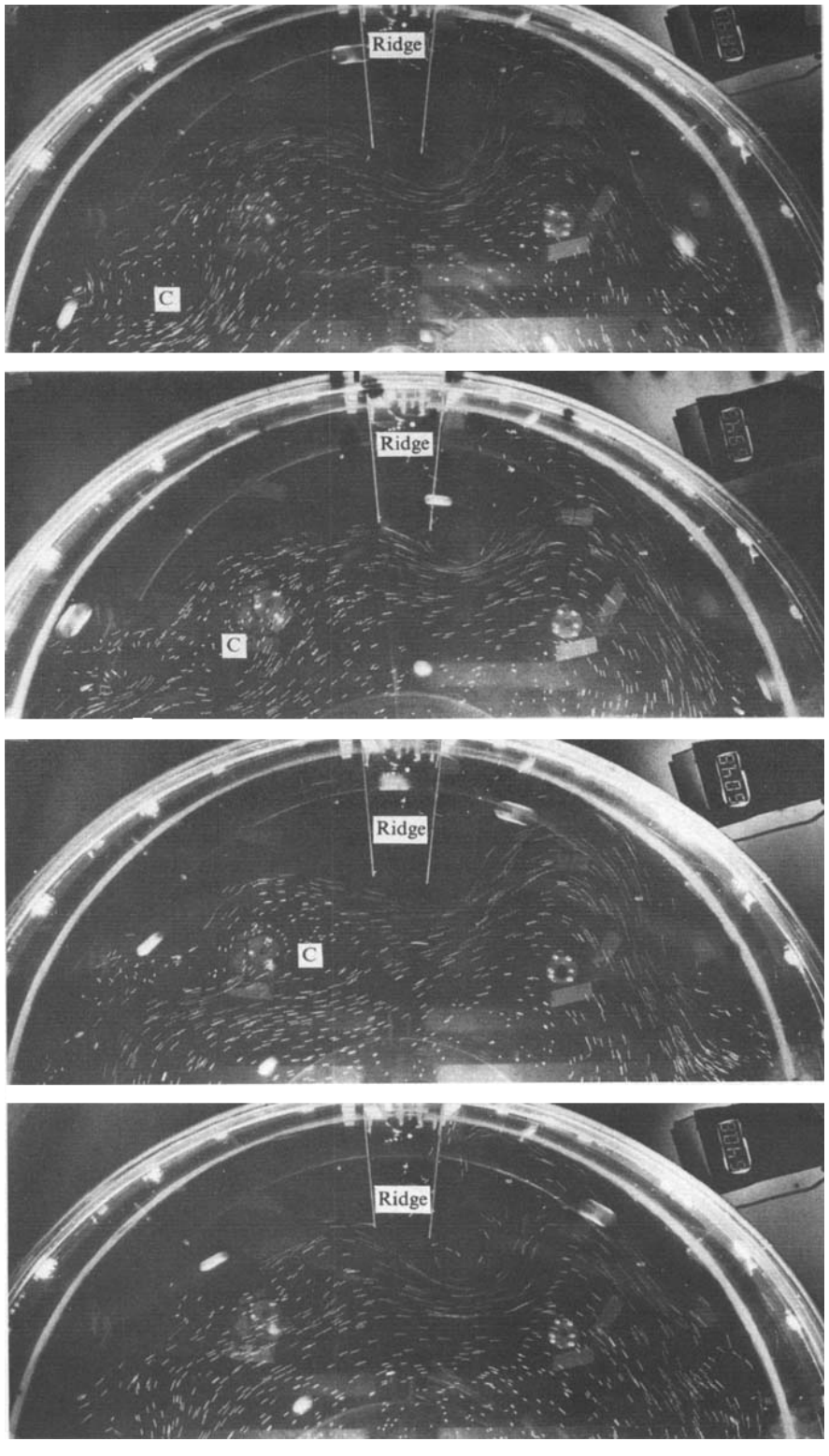

FIGURE 3. A set of streak photographs for parameter values of $f = 2.45$ rad/s, $g' = 23.54$ cm/s^2, $h_0 = 2.2$ cm and $\Delta\Omega \simeq 0.125$ rad/s. (*a*) was taken at $t \approx 589$ s and shows a pinched-off cyclone upstream of the ridge (indicated by the letter C). (*b*) and (*c*) were taken at $t \approx 594$ and 604 s respectively, and show the cyclone of photograph (*a*) drifting towards the ridge. Photograph (*d*) was taken at $t \approx 640$ s, and shows that the above-mentioned cyclone has been absorbed at the ridge.

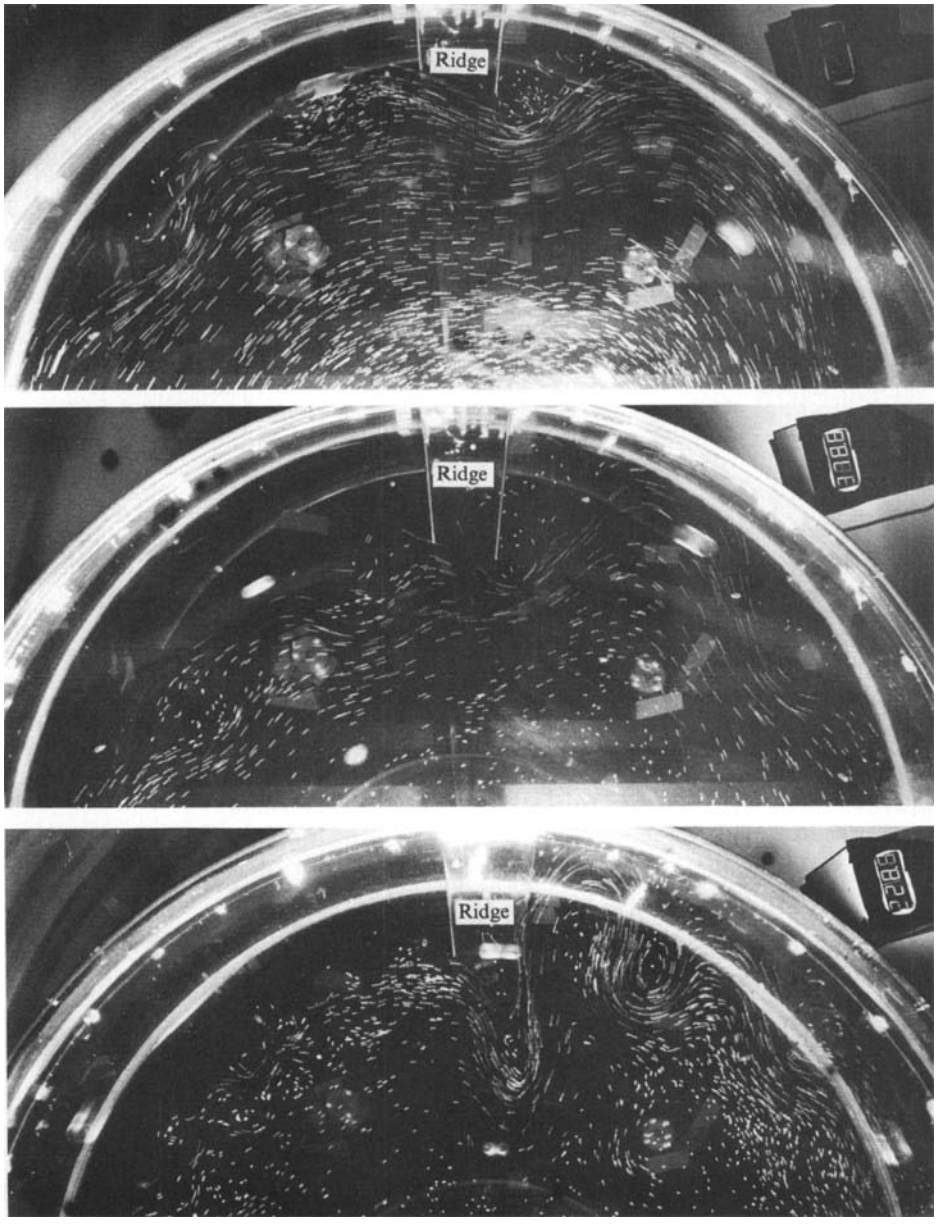

FIGURE 4. A set of streak photographs for parameter values of $f = 4.6$ rad/s, $g' = 20.12$ cm/s^2, $h_0 = 2.5$ cm and $\Delta\Omega \approx 0.125$ rad/s. They show the instability of the maximum plume at the ridge. (*a*) was taken at $t \approx 178$ s, the plume is becoming unstable and its amplitude is large. (*b*), taken two rotational periods later, shows that the cyclone is about to be pinched-off from the head of the plume. (*c*), taken two rotational periods later, shows the cyclone being pinched-off and the amplitude of the remaining plume being reduced to its normal value. Note that this process was repeated a number of times during the course of the experiment.

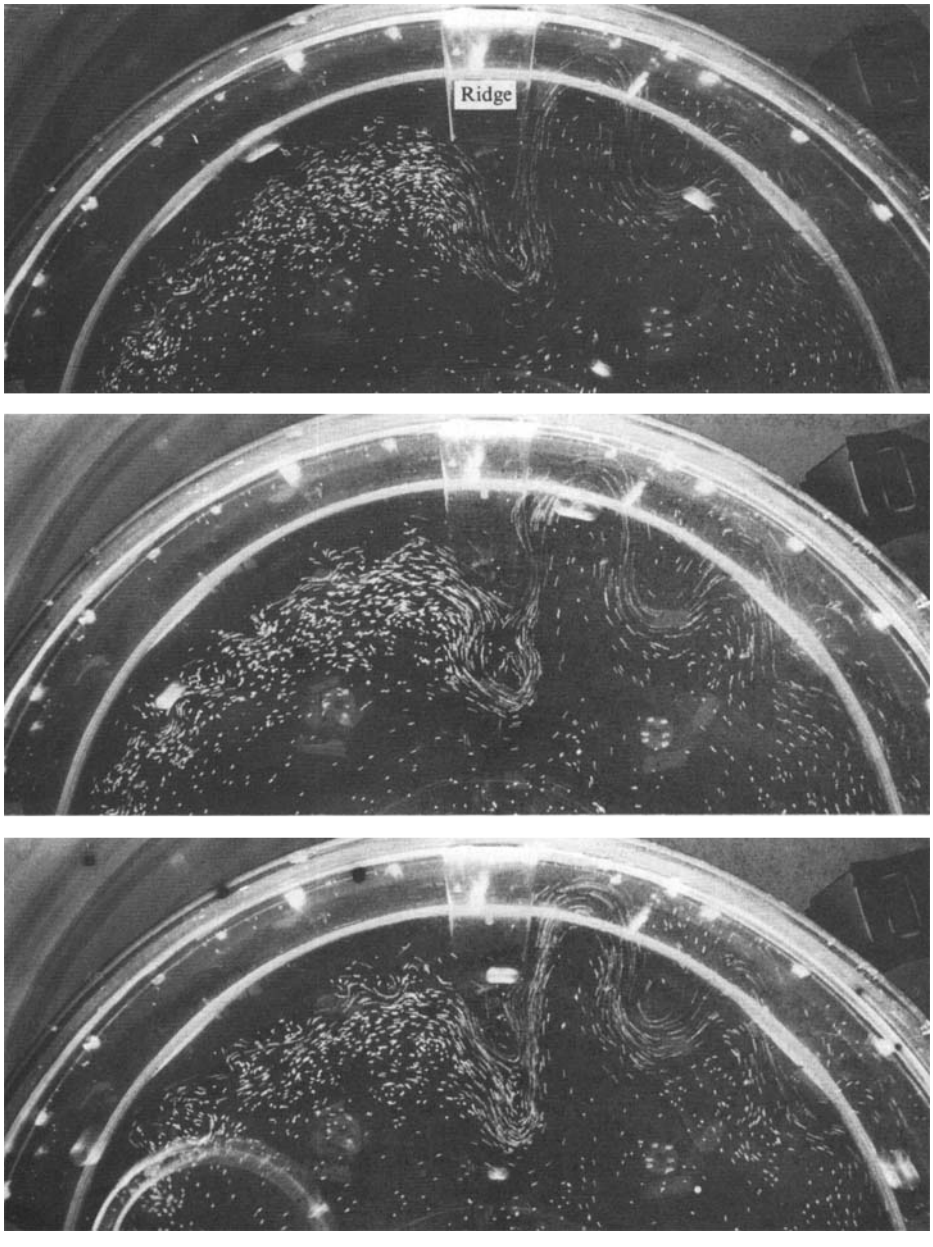

FIGURE 5. Streak photographs taken from three different experiments to compare the general character of the flow as the values of θ_* vary. For these experiments θ_* took the values of 16.35, 6.43, 2.57 for (*a*), (*b*) and (*c*) respectively. In these photographs, as the value of θ_* decreases, the large downstream standing wave forms closer to the maximum plume. Note the formation of smaller standing waves downstream of the large one in (*c*) with the value $\theta_* = 2.57$. The amplitude of the large standing wave is almost the same for all values of θ_*, while the length of the wave decreases as the value of θ_* decreases. In (*a*) and (*b*) the maximum plume is stable and contains a permanent cyclone, while in (*c*) the plume can become unstable to allow a cyclone to pinch-off from the head of the plume (see figure 4). Also note that, as the value of θ_* increases, the width of the plume increases. The wavelength of the upstream wave is greater in (*a*) than in (*b*) and (*c*), which indicates the size of the cyclone or anticyclone decreases as the value of θ_* decreases.

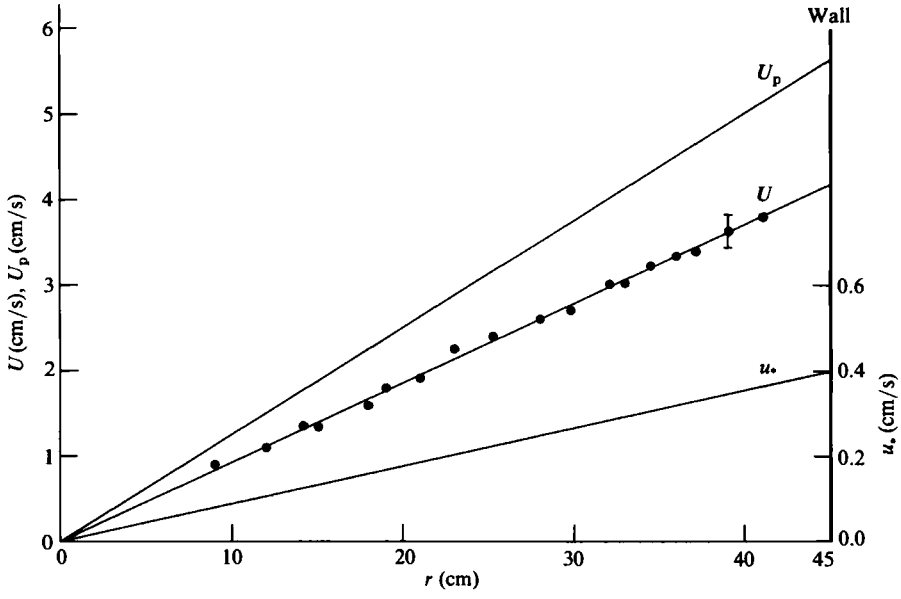

FIGURE 6. The top line is the variation of the known disk velocity $U_p = 0.125r$ with radius r, the middle line is the direct measurements of the top-layer mean velocity U from streak photography at different values of r, and the bottom line is the value of the disk friction velocity calculated from (2).

to that of the fully developed maximum plume. As f increased, the wavelength of the downstream standing wave decreased and successive waves were of smaller amplitude (see figure 5). This caused an occasional interaction between the plume and the first wave to produce a large trapped anticyclone near the downstream intersection of the ridge and the wall. This anticyclone lasted for a few rotation periods, and after that the usual jet pattern was observed (see figure 2).

4. Disk friction velocity

In order to be able to compare our results with field observations, it is useful to reduce the data using a universally accepted way of specifying the stress applied to the surface. Thus in this section we estimate the disk friction velocity u_* as a function of the known plate velocity $U_p = r\Delta\Omega$, so that u_* can be used as one of the independent parameters of the experiments. The idea is to make a direct measurement of the mean velocity U at the upwelling front in a steady-state situation for a given plate speed, and then to use the experimental observation of Kantha, Phillips & Azad (1977) or the experimental results of Narimousa, Long & Kitaigoridskii (1985) to estimate u_*. The observations by Kantha *et al.* suggested that $U \approx 10u_*$, and the direct estimate of Narimousa *et al.* based on 50 experiments indicated that $U \approx 10.6u_*$. The above-mentioned experiments were conducted in the absence of rotation; therefore an experiment with the lowest $f = 1.244$ rad/s used in this investigation was chosen to estimate u_*. Under these circumstances, rotational effects were small, the number of waves at the front was low, and therefore the aximuthal motion of the particle streaks could be used to measure U. Under these conditions, λ_s and the maximum η_s were small (about 4 cm). In this particular experiment the

steady state was reached after about 950 s, and measurements of U, based on the streak-photography picture, were taken after 1361 s to make sure that the flow was asymmetric and not, as in the earlier stages, under the blocking effect of the ridge. The results of this measurement are shown by the middle line of figure 6, while the top line is the plate velocity, and the bottom line shows the values of u_* obtained from $U \approx 10.6u_*$. According to figure 6, $U \approx 0.093r$, $U_p = 0.125r$, so that

$$U \approx 0.744U_p \tag{1}$$

and

$$u_* \approx 0.07U_p. \tag{2}$$

Since U_p is an independent variable, u_* can be calculated from (2) and can be used as the basic parameter of the experiment to model the wind friction velocity at the 'air–sea interface'. Kantha *et al.* have measured u_* and U_p directly, and find that, when the Richardson number $Ri_* = 36.3$, $u_* \approx 0.067U_p$, and when $Ri_* = 262.2$, $u_* \approx 0.071U_p$. These values are in good agreement with (2).

5. Theory

The present study employs a simple theoretical model similar to that of Linden & van Heijst (1984) to estimate the width λ_s of the upstream upwelled flow at the surface in a steady-state situation. As mentioned in §3, the Coriolis force associated with the anticyclonic azimuthal velocity of the top layer tends to cause the migration of the front away from the wall, while the build-up of a horizontal pressure gradient across the front due to the distortion of the interface opposes the Coriolis force and tends to stop the front. In the steady state these two effects balance. We ignore the effect of turbulent mixing and centrifugal pressure gradients, and assume that the upper layer is spun-up to the plate velocity, i.e. that the interfacial stress is small. In this condition, the front is in geostrophic balance, which implies

$$-fr\,\Delta\Omega = g'\frac{d\eta_s}{dr}, \tag{3}$$

where $r\,\Delta\Omega$ is the plate velocity, $f = 2\Omega$ is the Coriolis parameter, r is the radial coordinate measured from the origin at the centre of the tank, g' is the reduced gravity and η_s the depth of the front from the surface. Solving (3), we find

$$\frac{f\Delta\Omega\, r^2}{2g'} = \eta_s + c_1. \tag{4}$$

If R is the distance of the front (at the surface) from the centre of the tank, then, at $r = R$, $\eta_s = 0$ and, solving (4) with this boundary condition, we obtain

$$\eta_s = \frac{f\Delta\Omega}{2g'}(R^2 - r^2). \tag{5}$$

Conservation of the volume of the top layer implies that

$$2\pi \int_0^R \frac{f\Delta\Omega}{2g'}(R^2 - r^2)\, r\, dr = \pi h_0 R_0^2, \tag{6}$$

where h_0 is the initial depth of the top layer and R_0 is the tank radius. Solving (6) for R, we find

$$R = \left(\frac{4h_0 g' R_0^2}{f\Delta\Omega}\right)^{\frac{1}{4}}. \tag{7}$$

Since the width of the upwelled flow at the surface is $\lambda_s = R_0 - R$, solving (7) for λ_s, we find

$$\frac{\lambda_s}{R_0} = 1 - \left(\frac{4g'h_0}{f\Delta\Omega R_0^2}\right)^{\frac{1}{4}}. \tag{8}$$

In terms of the maximum friction velocity U_* at the outer edge of the disk, (8) becomes

$$\frac{\lambda_s}{R_0} = 1 - \left(\frac{g'h_0}{3.58fU_* R_0}\right)^{\frac{1}{4}}, \tag{9}$$

where $U_* = R_0\Delta\Omega/14.3$ is based on (2). The calculated values of λ_s from (9) are in good agreement with the measured values of λ_s, and, as will be seen in §6, will be used as the lengthscale in the present study. When $\lambda_s = 0$, (9) reduces to

$$\frac{g'h_0}{fU_* R_0} = 3.58. \tag{10}$$

This condition implies that $g'h_0/fU_* R_0 < 3.58$, the outer edge of the front migrates away from the wall and allows the bottom fluid to appear at the surface. For values of $g'h_0/fU_* R_0 > 3.58$, although the bottom fluid upwells near the wall, it does not appear at the surface.

To find a relationship for η_s based on the initial parameters of the experiments, we substitute (7) into (5), and this yields

$$\frac{\eta_s}{h_0} = 7.15\left(\frac{g'h_0}{fU_* R_0}\right)^{-1}\left(-\frac{r^2}{R_0^2}\right) + 3.78\left(\frac{g'h_0}{fU_* R_0}\right)^{-\frac{1}{2}}. \tag{11}$$

At the centre of the tank $r = 0$, and (11) reduces to

$$\frac{\eta_m}{h_0} = 3.78\left(\frac{g'h_0}{fU_* R_0}\right)^{-\frac{1}{2}}, \tag{12}$$

where η_m is the maximum value of η_s at the centre of the tank. In other words, (13) gives maximum lowering of the interface due to the spin-up process of the top layer. For the critical condition (10), (12) becomes

$$\eta_m = 2h_0. \tag{13}$$

This condition indicates that only when the maximum lowering of the interface η_m is greater than twice the initial depth h_0 ($\eta_m > 2h_0$) will the front migrate away from the outer edge of the tank.

6. Results

6.1. *Migration rate of the upstream front*

As described in §3, during the spin-down of the top layer the interface deformed, and, after intersecting the surface of the disk, began to migrate away from the wall. The distance between the front and the wall is denoted by λ. In figure 2 the region without particles indicates this width, and was measured for a number of experiments. The measured values of λ in a given experiment are plotted as a function of time in figure 7. These plots indicate that, in all experiments, λ increases linearly with time until $\lambda = \lambda_s$, after which the front is stationary. The results on figure 7 also indicate that, as f increases, the front migrates faster. The slope of the linear growth of λ with time t is called the speed of front migration u_f. The solid lines parallel to the t-axis on figure 6

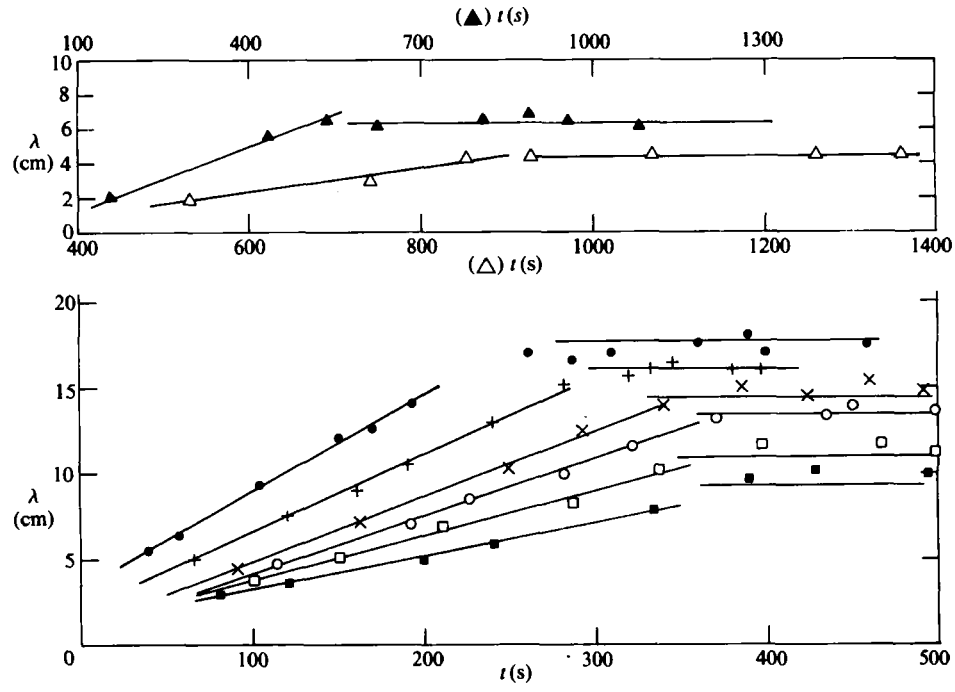

FIGURE 7. Variations of the width λ of the upwelled layer at the surface with time at various θ_* values. The solid lines parallel to the t-axis are calculated values of λ_s from (10). The key is as follows:

	f (rad/s)	h_0 (cm)	$\Delta\rho_0$ (g cm^{-3})	u_* (cm s^{-1})	λ_s (cm)	u_f (cm/s)	θ_*
▲	1.244	2.25	0.024	0.36	4.42	0.0072	26.77
△	1.5	2.25	0.024	0.344	6.28	0.012	16.35
■	1.94	2.1	0.024	0.318	9.32	0.02	8.6
□	2.45	2.2	0.024	0.3	10.94	0.026	6.43
○	3.0	2.4	0.02	0.28	13.38	0.0344	4.2
×	3.5	2.35	0.0205	0.272	14.55	0.038	3.42
+	4.6	2.5	0.0205	0.26	16.12	0.045	2.57
●	5.82	2.6	0.02	0.24	17.67	0.05	2.03

where the values of u_* are estimated at the stationary front. Note that a given value of λ is averaged over 3–5 rotation periods and has an error of about 10%.

are the calculated values of λ_s from (10), and they are in good agreement with the measured values.

To classify these results, on dimensional grounds we can write simply

$$F = F'(\Delta\Omega, f, g', h_0, R_0, \alpha), \tag{14}$$

which indicates that any given measured quantity must be a function of the initial parameters of the experiments, and we assume the processes at the front are inviscid. It is more convenient to introduce u^* as a velocity scale and λ_s as a lengthscale, so that u_f, for example, is

$$u_f = u_f(u_*, f, g', h_0, \lambda_s, \alpha). \tag{15}$$

As a first attempt to find this functional dependence of u_f, we have simply made a plot of migration rate u_f/u_* as a function of buoyancy force over Coriolis forces $\theta_* = g'h_0/u_* f\lambda_s$ using λ_s as the lengthscale. When the values of u_* at the position of the steady-state front are used to scale the measurements, the results are shown in

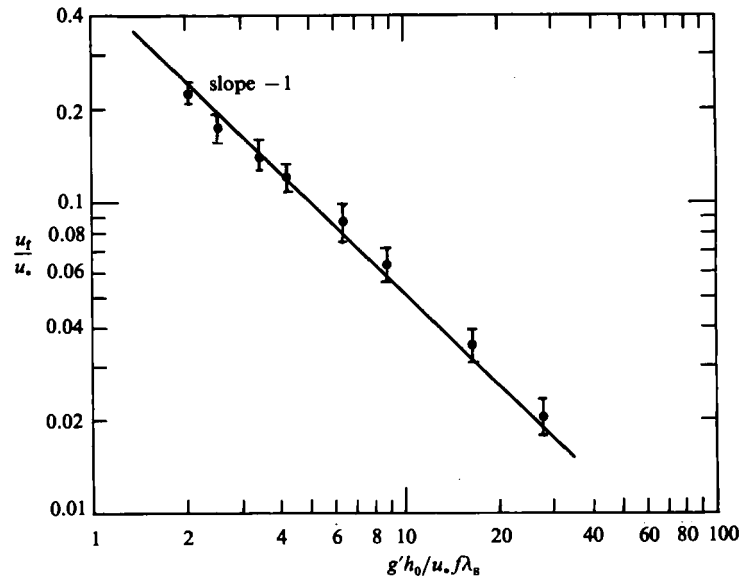

FIGURE 8. The variation of migration rate of the front at the surface u_f/u_* with θ_*. See the caption of figure 7 for values of the parameters.

figure 8. These results indicate that, as the value of θ_* increases, the migration rate u_f/u_* decreases. According to figure 8 we can write

$$M_f = \frac{u_f}{u_*} = 0.5\left(\frac{g'h_0}{u_* f\lambda_s}\right)^{-1}. \tag{16}$$

Solving (16) for λ, we find

$$\lambda = 0.5\left(\frac{g'h_0}{u_* f\lambda_s}\right)^{-1} u_* t, \tag{17}$$

which gives the linear dependence of λ as a function of time t. At steady state, $\lambda = \lambda_s$, and (17) reduces to

$$t_s = \frac{2g'h_0}{fu_*^2}, \tag{18}$$

which gives the timc t_s to reach a steady state. An interesting consequence of this comes from writing (18) in terms of the rotation rate Ω as follows:

$$\Omega t_s = \frac{g'h_0}{u_*^2} = Ri_*, \tag{19}$$

where Ri_* is the Richardson number. This result implies that the upstream front becomes stationary whenever the kinetic and potential energy are balanced. We note also that θ_* is a product of a non-dimensional Rossby deformation radius $\theta = (g'h_0)^{\frac{1}{2}}/f\lambda_s$ and the Richardson number to the power $\frac{1}{2}$, so that the migration rate M_f becomes

$$M_f = 0.5\theta^{-1}Ri_*^{-\frac{1}{2}}, \tag{20}$$

while (17) can also be written as

$$\frac{\lambda}{\lambda_s} = \Omega t\, Ri_*^{-1}. \tag{21}$$

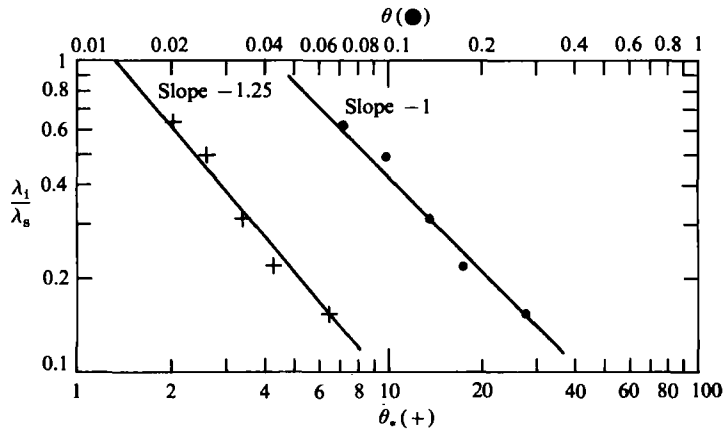

FIGURE 9. The variation of λ_i/λ_s with θ_* (+), and the Rossby deformation radius $\theta = g'h_0/f\lambda_s$ (○).

6.2. *A criterion for the appearance of upstream baroclinic waves*

We have already described in §3 that at some point during the migration of the front, when $\lambda = \lambda_i < \lambda_s$, i.e. before a steady state is reached, non-asymmetric disturbances (baroclinic waves) appear at the front.

To estimate the condition at which these waves appear, we have plotted in figure 9 λ_i/λ_s as a function θ_*, for five experiments in which we have been able to detect the first appearance of the waves. From figure 9 we can write

$$\frac{\lambda_i}{\lambda_s} = 1.56\theta_*^{-1.25}. \tag{22}$$

Waves always appear at the front for values of λ_i smaller than λ_s, which sets a limiting value on $\theta_* = \theta_{*L}$ when $\lambda_i = \lambda_s$ of

$$\theta_{*L} = 1.44. \tag{23}$$

This limiting condition (23) indicates that waves always appear at the front when the value of $\theta_* > 1.44$.

In figure 9 we plot λ_i/λ_s as a function of non-dimensional Rossby deformation radius θ, and we can write

$$\frac{\lambda_i}{\lambda_s} = 0.041\theta^{-1}, \tag{24}$$

with the extreme condition $\lambda_i = \lambda_s$ giving

$$\theta_L = 0.041. \tag{25}$$

It can be seen from (22) and (24) that, to the accuracy of these experiments, the occurrence of baroclinic waves can depend on either θ_* or θ, and at this stage we cannot decide which is correct. We note that, owing to experimental limitations, the variations of the values of the Richardson number $410 \leqslant Ri_* \leqslant 885$ and the Rossby deformation radius $1.23 \leqslant L_R \leqslant 5.85$ were quite small. This was the result of the fact that (i) the disk velocity had to be kept low in order to minimize turbulent mixing; (ii) we were limited in the range of rotation rates, since large values gave strong centrifugal effects which resulted in large deformations of the initial interface; (iii)

owing to the large density of the particles used to identify the flow field, we were limited in our choice of the values of initial density jump $\Delta\rho_0$; (iv) it was easier to observe the first appearance of the waves at the upstream front in the experiments with lower values of θ_*, since at higher values the waves occurred very close to the wall of the tank. All of these problems limited the number of data points on figure 9. In future work (Narimousa & Maxworthy 1985) we hope to overcome some of these problems and find a universal criterion to predict the occurrence of the baroclinic waves at the upstream front.

The stability of such fronts in a rotating two-layer stratified fluid has been investigated previously by Saunders (1973), Griffiths & Linden (1981) and Hart (1972, 1980). Saunders placed a salt solution inside a bottomless cylinder of height h_0, which was placed sealed centrally in a large basin filled with fresh water. After the system was brought to solid-body rotation the cylinder was lifted out vertically, allowing the denser fluid to collapse and spread radially, until a quasigeostrophic balance was reached. In these experiments the released potential energy due to buoyancy forces is the source of kinetic energy in the amplifying baroclinic instabilities. Saunders described the instability of the asymmetric flow by considering a range of values of $\theta_0 = (g'h_0)^{\frac{1}{2}}/fR_0$ (where R_0 is the cylinder radius). He found that when $\theta_0 < 1.35$ the asymmetric flow becomes unstable to baroclinic instabilities.

Griffiths & Linden (1981) repeated Saunders' experiment, but this time the inner cylinder was filled with a fluid lighter than the environment, so that the vortex was formed at the free surface rather than on the bottom. They found that the surface vortices were always unstable to a minimum wavenumber $n = 2$, and n increased as the values of θ_0 decreased. A stable bottom vortex and vortex-wandering ($n = 1$) were observed in Saunders' experiments, while these features were absent in the surface vortices of Griffiths & Linden's experiments. Griffiths & Linden argued that the existence of the bottom vortices in Saunders' expersiment could result from the viscous decay of long waves due to the bottom Ekman layer, which is absent at the free surface. However, they found that transition to instability occurred at smaller values of θ_0, compared with the values found by Saunders ($\theta_0 \geqslant 1$). For example, the wavenumber $n = 2$ occurred at values of $\theta_0 = 0.56$ in Griffiths & Linden's experiments, while the same wavenumber occurred at values of $\theta_0 = 0.89$ in Saunders' experiments.

In general, the above-mentioned experiments did not find a universal criterion for transition from stability to instability. This suggests that the single dimensionless parameter θ_0 is not the only parameter determining transition, and that there is another parameter θ_* which may also be important in determining the stability of the asymmetric front.

In the experiments of Griffiths & Linden and Saunders the buoyancy force was the driving mechanism, and tended to spread the less-dense flow radially at the surface or the denser flow at the bottom. The Coriolis force associated with the azimuthal velocity of the basic vortex opposed the build-up of the radial pressure gradient due to buoyancy forces and tended to stop the radial flow. In the present experiments the processes were somewhat different from those mentioned above. After the stress was applied to the top surface, the Coriolis force associated with the spin-up of the azimuthal velocity of the top layer tended to distort an initially stable situation and to build up a pressure gradient to oppose the Coriolis force.

Griffiths & Linden (1983) have also reported experiments in which a continuous supply of fluid from a confined source was released into an environment with different density which was in solid-body rotation. They found that the initially asymmetric flow became marginally unstable when $\theta_0^2(\delta/(1-\delta))^{-\frac{1}{2}} \approx 0.02$ for values of

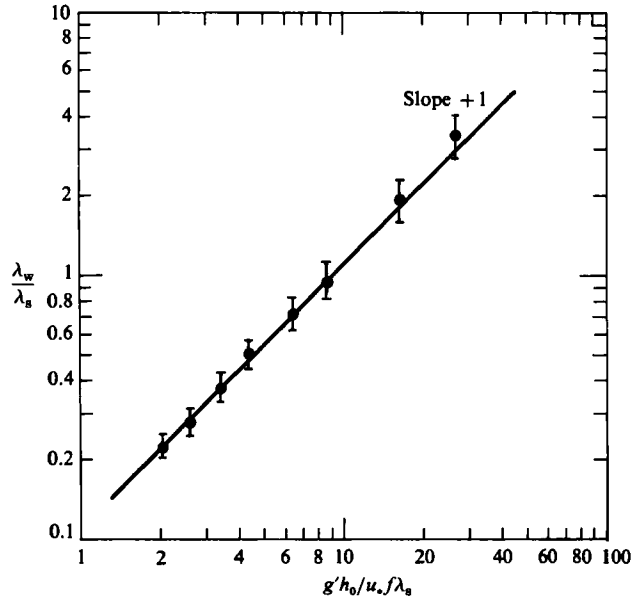

FIGURE 10. The variation of λ_w/λ_s with θ_*, where λ_w is the size of a frontal cyclone or anticyclone.

$\delta = h/H > 0.2$ (H is the total depth of the flow and h is the maximum depth of the vortex). For values of $\delta < 0.2$ they found that vortices can be unstable at values of $\theta_0^2(\delta/(1-\delta))^{-\frac{1}{2}}$ significantly greater than 0.02. They reported that for these small depth ratios extraction of kinetic energy from the basic shear was the dominant driving mechanism in growth of instabilities. In our experiments the value of δ was always greater than 0.2, but the shear due to the applied stress at the surface was the source of kinetic energy for the growth of the waves. In fact the velocity jump across the front gave rise to Kelvin–Helmholtz instabilities, which are a consequence of shear at the density front, and may then be responsible for the growth of waves at the edge of the asymmetric front (see also Griffiths & Linden 1982).

The critical conditions (23) and (25) for waves to appear at the front were found for the cases in which the top layer was relatively thin and the edge of the density front intersected the rotating top disk. For cases in which the density front does not intersect the horizontal boundary, the reader is referred to Hart (1972, 1980).

6.3. *Size of the upstream waves*

When circular waves (cyclones and anticyclones) appeared at the front when it was at a distance $\lambda_i < \lambda_s$ from the wall, we measured their average size λ_w, where λ_w is the average diameter of a frontal cyclone or anticyclone. Our measurements and observations for a given experiment indicate that the measured values of λ_w at $\lambda = \lambda_i$ were almost equal to the measured values of λ_w at $\lambda = \lambda_s$ when the front was stationary. These measured values of λ_w were then made non-dimensional by λ_s and are plotted against θ_* in figure 10. According to these plots, we can write

$$\frac{\lambda_w}{\lambda_s} \approx \frac{g'h_0}{10u_*f\lambda_s} = \tfrac{1}{10}\theta_* \tag{26}$$

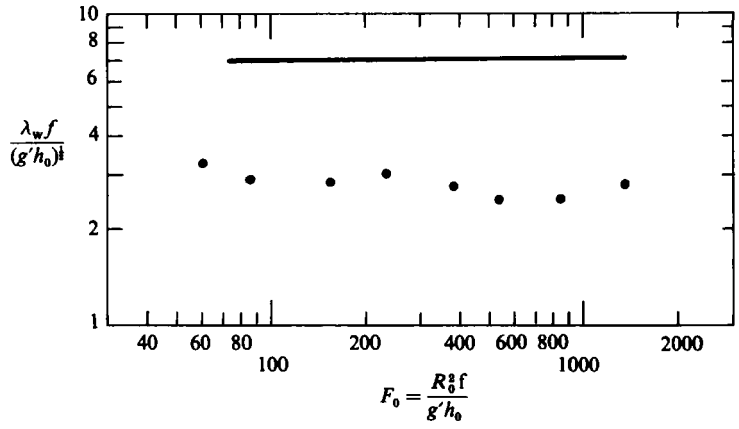

FIGURE 11. The size of the waves λ_w normalized by Rossby deformation radius L_R and plotted *vs.* initial Froude number F_0. The solid line parallel to the F_0 axis shows the average values of the data taken from Griffiths & Linden's (1982) figure 0.

or
$$\lambda_w \approx \frac{g'h_0}{10u_* f}, \tag{27}$$

so that the size of the waves at the upwelling front is independent of the final width λ_s of the upwelled flow at the surface. Using (1) and (2) to substitute for u_*, (27) becomes

$$\theta_w = \frac{g'h_0}{Uf\lambda_w} \approx 1. \tag{28}$$

Griffiths & Linden (1982) generated a rotating two-layer stratified flow near a vertical wall by withdrawing the inner wall of an annulus with a narrow gap, and allowing the fresh water within the annulus to collapse into the denser environment. They observed growing wave-like disturbances on the density front. They measured the wavelength $L_w = 2\lambda_w$ of the growing waves, non-dimensionalized them with the initial Rossby deformation radius $R_L = (g'h_0)^{\frac{1}{2}}/f$ and plotted them against the initial Froude number $F_0 = f^2L^2/g'h_0$ (where L_0 is the initial width of the fresh water). Their results showed that for values $F_0 \gtrsim 20$ the size of the waves was independent of F_0, and on the average $\lambda_w/R \approx 3.5$. To compare our experimental results with theirs, we show our data on figure 11, where R_0 has been used in our data compared with L_0 in their data. Our results indicate that, for the range $59 < F_0 < 1336$ in which our experiments were conducted, the value of λ_w/R_L is also independent of F_0 and gives $\lambda_w/R \approx 3$, about 10% smaller than the Griffiths & Linden result. It usually took a number of rotation periods to see a change in the size of the waves, and in our experiment by that time the wave had reached the ridge and had vanished. Of course, in experiments in the absence of the ridge we should expect the size of the wave to grow larger than in those with the ridge. In this case we would expect to get better agreement between the value of λ_w/R and that of Griffiths & Linden (1982). These results will be published in detail at a later date (Narimousa & Maxworthy 1985).

6.4. *Drift velocity of the upstream waves*

Once the waves were generated upstream, they propagated in the direction of the applied stress towards the ridge. The average drift velocity u_w of the waves was

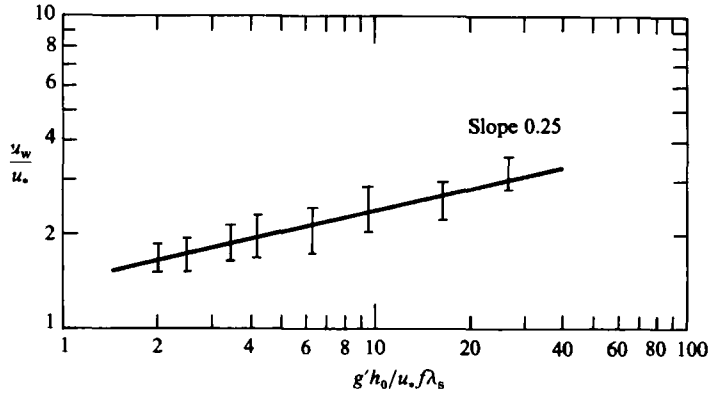

FIGURE 12. The variation of the drift velocity of the upstream waves with θ_*.

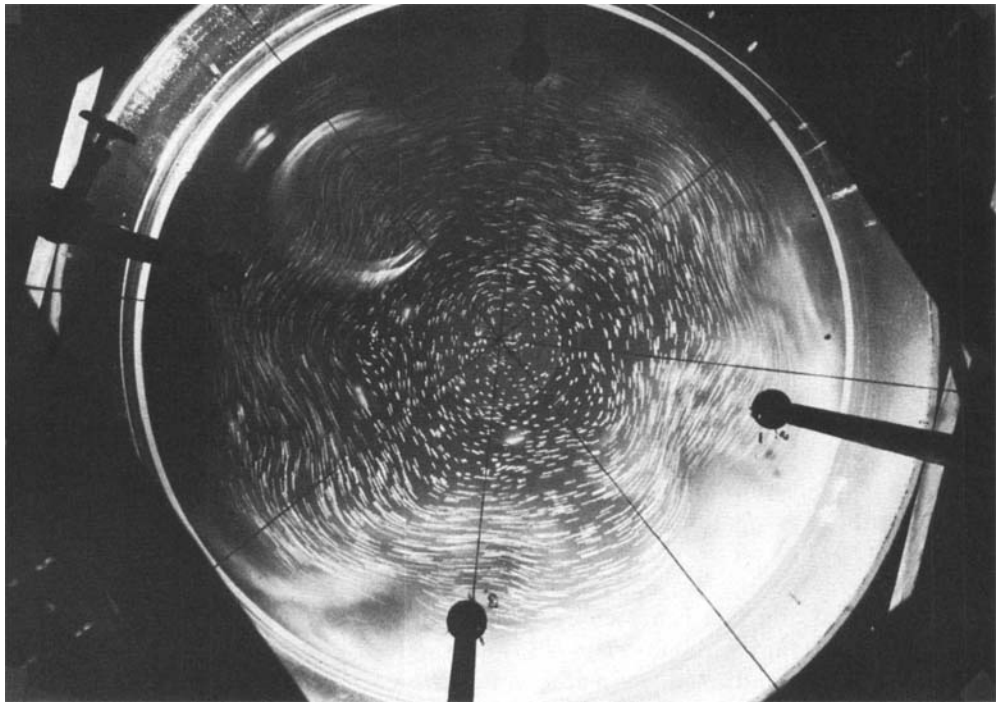

FIGURE 13. A photograph taken from an experiment with a value of $\theta_* \approx 6$ in the absence of the bottom topography and the conical bottom. Note that the circular form of the cyclone and anticyclones is absent in the photograph, indicating that the waves drift considerably faster than those formed in the presence of bottom topography.

measured by tracing the displacement of a particular wave for a few rotation periods. For example, in figure 3 we show a sequence of pictures in which one particular wave is seen to drift downstream. The total distance that the wave has drifted, was then divided by $t = m\Omega^{-1}$ (where m was the number of rotational periods during which the wave was traced) to obtain the experimental values of u_w. The measured values

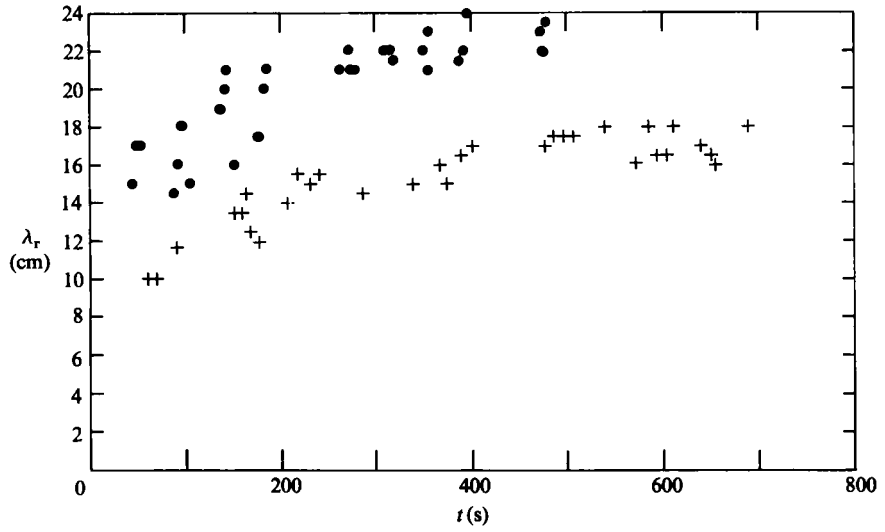

FIGURE 14. The variation with time of the width λ_r of the upwelled flow at the surface at the ridge, for the experiments with $\theta_* = 2.03$ (○) and $\theta = 36.43$ (+). The scattering of the data is due mainly to vacillation of the plume.

of u_w were non-dimensionalized by u_* and are plotted against the values of θ_* on figure 12, from which we can write approximately

$$\frac{u_w}{u_*} \approx 1.5\theta_*^{0.25}. \tag{29}$$

This, when combined with (27), indicates that at high values of θ_* the large waves that are formed travel faster than the smaller waves corresponding to low values of θ_* (see also the results of the heated annulus experiments of Douglas *et al.* (1972), who also found that larger waves at low values of f travelled faster than the smaller waves at high values of f).

At low values of θ_* the smaller waves were generated farther away from the wall, where the disk velocity was smaller, and this could partly explain this result. However, we believe that the main effects are due to rotation and the presence of the ridge (see figure 13).

6.5. *Upwelling on the ridge*

After the stress was applied to the top surface, we observed that the bottom fluid first appeared as a jet or plume at the surface over the ridge. A few rotation periods later, the bottom fluid then appeared at the surface, upstream of the ridge. As the experiment continued, the head of this plume always migrated in advance of the upstream front to produce always a maximum upwelling on the ridge. The maximum excursion of the plume (maximum upwelling) was always observed downstream of the front edge of the topography, while a cyclone was always observed within the plume. The numerical model of Preller & O'Brien (1980) and Ikeda & Emery (1984, see their figure 16) is consistent with these observations.

The distance λ_r of the head of the plume from the wall was measured from photographs like figure 2 and is plotted against the corresponding time on figure 14. The scatter of these plots is the result of a strong vacillation of the plume, which made

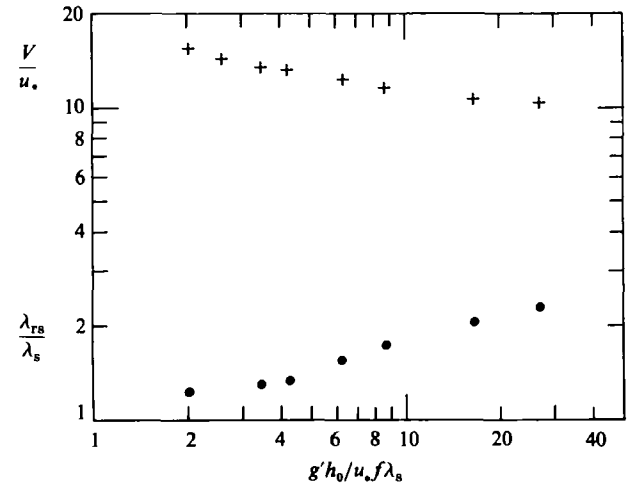

FIGURE 15. The top data (+) are the variation of the values of V/u_* (V is the average velocity measured at the inner edge of the jet) with θ_*. The bottom data (○) are the variations of the values of λ_{rs}/λ_s (λ_{rs} is the final width of the upwelled flow at the ridge) with θ_*.

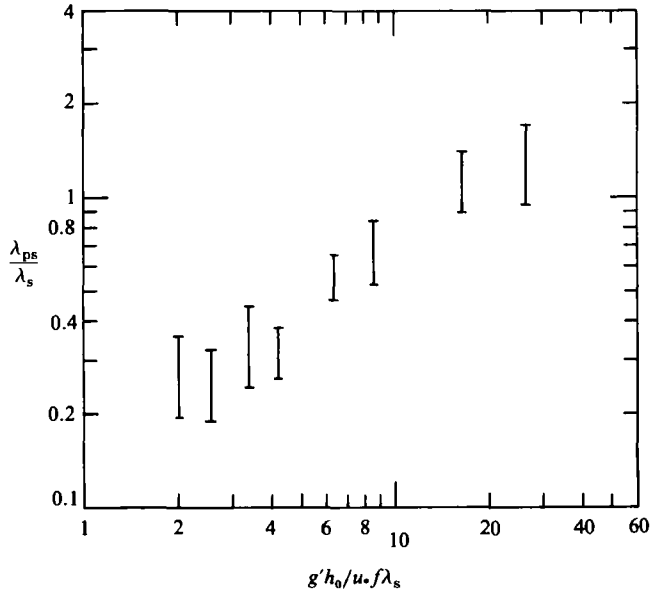

FIGURE 16. The variation of λ_{ps}/λ_s (λ_{ps} is the amplitude of the plume in the steady-state condition) with θ_*; vacillation of the maximum plume is indicated by the bars.

it difficult to measure λ_r. In general, as seen on figure 14, the average migration rate of the front on the ridge is constant. In the final stage when a steady-state condition was reached, the front became stationary, but it continued to vacillate about its steady-state value λ_{rs}. A comparison between figure 14 and the position of the upstream front on figure 7 for the same experiment indicates that the upstream front and the front on the ridge reached their steady-state values at about the same time.

At the steady-state condition, we measured the mean particle velocity V at the

edge of the plume at the density front, and found it did not vary despite large changes in f at constant $\Delta\Omega$ for the eight experiments reported here. The values of λ_{rs}/λ_s are plotted against θ_* on figure 15, from which we can write

$$\frac{\lambda_{rs}}{\lambda_s} \approx \theta_*^{0.25}. \tag{30}$$

These results can be presented in a slightly different way by plotting λ_{ps}/λ_s (where $\lambda_{ps} = \lambda_{rs} - \lambda_s$ is the amplitude of the plume in a steady-state condition) against θ_* as in figure 16. From this figure we have

$$\frac{\lambda_{ps}}{\lambda_s} \approx 1.2\,\theta_*^{0.75} \tag{31}$$

which is an approximation to the result, from (30) and the definition of λ_{ps}, that

$$\frac{\lambda_{ps}}{\lambda_s} = \theta_*^{0.25} - 1.$$

The result (31) indicates that an increase in θ_* results in an increase in λ_{ps}, which means that the effect of the ridge is stronger when the upstream front is closer to the wall. At low values of θ_* when the values of λ_s are large and the front is far from the wall, the effect of the ridge on the upstream front is weaker, i.e. the values of λ_{ps} are smaller, probably owing to the fact that the height of the ridge gradually decreases outward.

At high values of θ_* the plume was stable, while at low values $\theta_* \leqslant 2.6$ the head of the plume became unstable and gave rise to a pinched-off cyclone. In this process the amplitude of the plume first increased and the head of the plume narrowed to allow the bottom fluid to penetrate further outward. The cyclone then pinched-off from the plume and penetrated into the lighter fluid on the ridge, leaving a smaller-amplitude plume. We have observed the cyclone for a few rotation periods close to the reformed head of the plume, but later the cyclone is absorbed into the jet. These processes of instability of the plume, appearance of the cyclone, the pinch-off process and absorption of the cyclone are shown on figure 4.

6.6. *Flow downstream of the ridge*

We mentioned in §3 that the presence of the ridge caused a dramatic change in fluid motion on and downstream of the ridge. A jet-like motion away from the tank wall was produced on the ridge and consisted of a plume of upwelling maximum as already discussed in §6.5. Beyond the ridge, and especially at lower values of θ_*, the jet turned abruptly and flowed back towards the wall and parallel to the ridge, until it reached the wall of the tank. The jet then turned and gave rise to a number of large standing waves further downstream. It took about 10–15 initial rotation periods for the standing wave to develop fully, and its amplitude A_{sw} (see figure 2*d*) was always greater than λ_{ps}, that of the plume, while the values of A_{sw} were always smaller than λ_{rs}.

At the higher values of θ_* the maximum of the standing wave was far downstream of the ridge (see figure 5*a*). At these high values of θ_* that part of the jet between the plume maximum and the standing wave flowed parallel to the wall and almost no upwelling was observed in this location (see figure 5*a*). The only area of upwelling downstream of the ridge was observed to occur within the cyclones making up the crests of the standing waves.

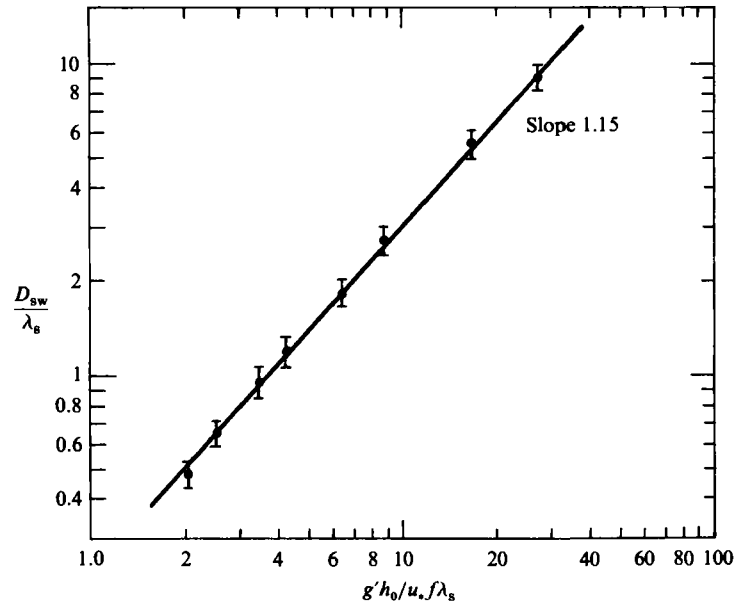

FIGURE 17. The variation of D_{sw}/λ_s (D_{sw} is the distance of the large standing wave from the maximum plume) with θ_*.

As the value of θ_* decreased, the distance between the standing waves was observed to decrease and occur closer to the ridge (see figure 5*c*). This caused an occasional interaction between the plume maximum and the first standing wave and the production of a large anticyclone between them (see figure 5*c*). This was observed for a few rotation periods and then disappeared. The measured mean velocity V around the inner edge of the jet downstream of the ridge was virtually constant and equal to that found previously in the plume, so that the correlation found previously (figure 15) was still valid.

If the distance of the maximum of the first standing wave crest from the maximum plume is denoted by D_{sw}, we can plot D_{sw}/λ_s against θ_* as on figure 17. From this we deduce

$$\frac{D_{sw}}{\lambda_s} \approx 0.22\theta_*^{1.15}. \tag{32}$$

However, if the exponent of θ_* is assumed to be unity, which gives errors in D_{sw} of about 20 % at the extreme values of θ_*, we can then write

$$\theta_{sw} = \frac{g'h_0}{u_* f D_{sw}} \approx 5.0. \tag{33}$$

After about 10–15 rotating periods the first standing wave was fully developed and its amplitude A_{sw} remained constant. This is demonstrated in figure 19, where we plot the values of A_{sw} as a function of time t. The scattering of the data is due to vacillation of the wave. We found that, as the values of θ_* decreased, the values of A_{sw} almost remained constant. Only at low values of $\theta_* \leqslant 2$ did the amplitude of the wave begin to increase, which caused the wave to become unstable, and in a similar fashion to the behaviour of the maximum plume a cyclone was pinched-off from the crest of the wave (see figure 18). Observation of such a pinch-off cyclone downstream

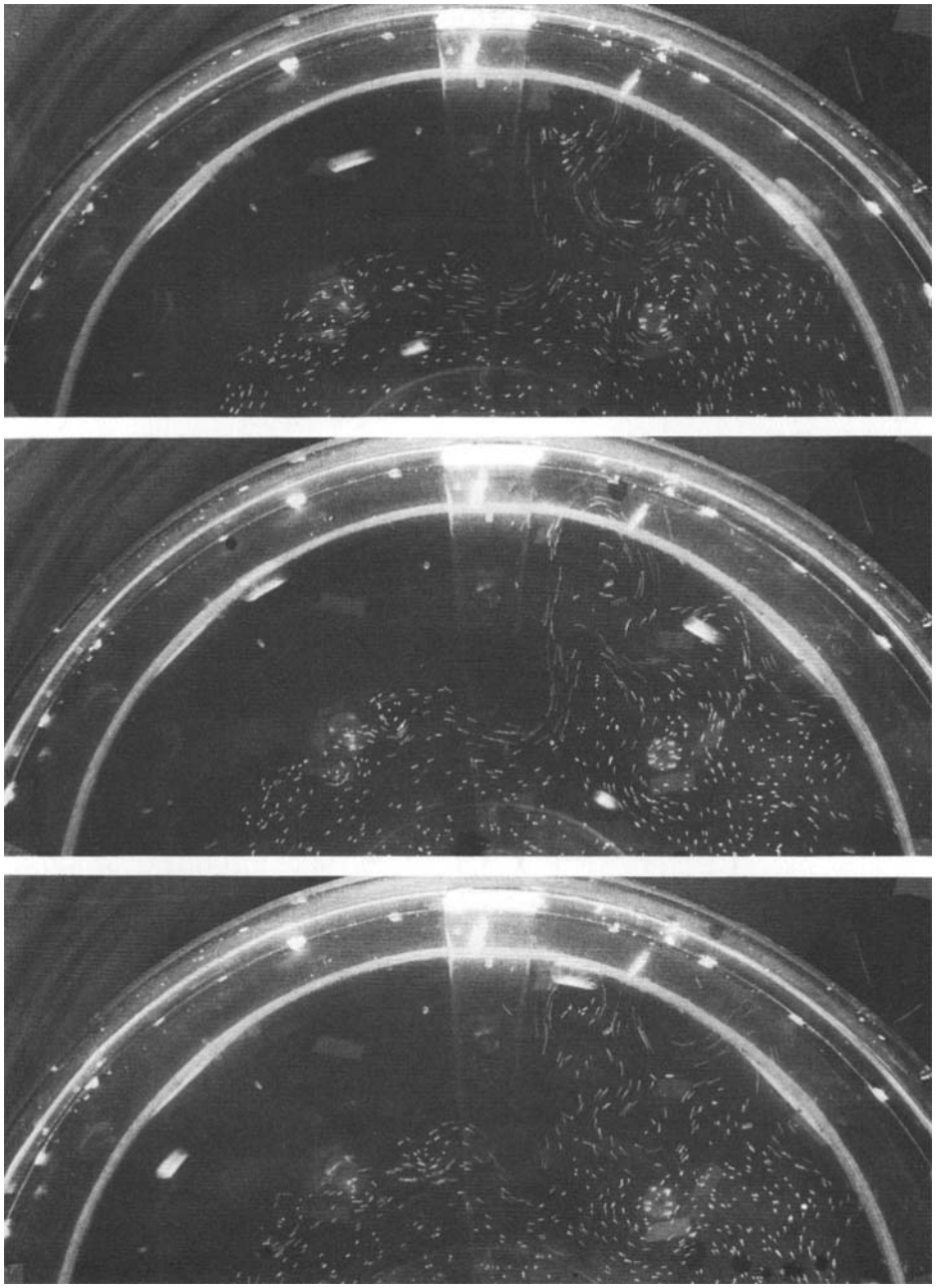

FIGURE 18. A set of streak photographs taken from the experiment with $f = 5.82$ rad/s, $h_0 = 2.6$ cm, $g' = 19.62$ cm s^{-2} and $\Delta\Omega = 0.125$ rad/s. In (*a*) the amplitude of the downstream standing wave has increased considerably, and in (*b*) the wave becomes unstable and a cyclone has pinched-off from the crest of wave (see (*c*)). Also note the trapped anticyclone near the downstream edge of the ridge close to the wall tank. Note that there is a difference of about two rotational periods between each of the photographs (*a*)–(*c*).

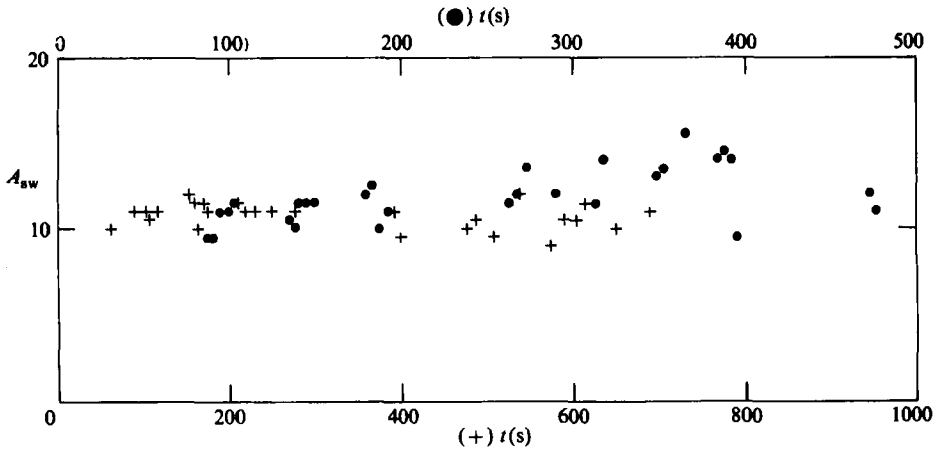

FIGURE 19. The variation with time of the amplitude A_{sw} of the downstream standing wave for the experiments with $\theta_* = 2.03$ (●) and $\theta_* = 6.43$ (+). The scattering of the data is due to vacillation of the waves. Note that the value of A_{sw} (for the experiment with $\theta_* = 2.03$) at about $700 < t < 800$ is increased, and becomes unstable to allow a cyclone to be pinched-off from the crest of the standing wave.

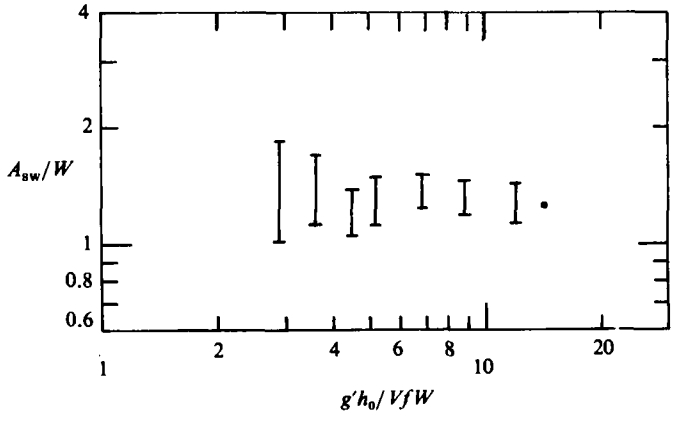

FIGURE 20. The variation of the amplitude of the downstream standing wave A_{sw}/W (W is the maximum width of the ridge) with $g'h_0/VWf$. The range of vacillation of the waves is indicated by the bars.

of Mendocino ridge has recently been reported by Rienecker *et al.* (1985). The cyclone then counter-rotated with the trapped anticyclone to produce an outward-meandering jet, similar to that reported by Mooers & Robinson (1984). The pinch-off timescale of the standing wave was considerably greater than for that of the maximum plume. The cyclone was observed for a few rotation periods and then disappeared. This effect is indicated on figure 19 for an experiment with $\theta_* \approx 2$, where at about $t \approx 750$ s, where the amplitude of the wave has increased to about $A_{sw} = 15.5$ cm, the cyclone has pinched-off and the amplitude of the standing wave is reduced. Changes in the value of θ_* caused the position of the standing wave to change, while its amplitude remained almost the same. Because of this, we suggest that it is the size of the ridge, which is kept the same for all experiments, that controls the amplitude of the stable

standing waves. If so, we can then use the maximum width W of the ridge at the wall to scale measurements of A_{sw}. In figure 20 we show plots of A_{sw}/W against the values of $g'h_0/VfW$, where the magnitude of the vacillation of the waves is indicated by the bars.

We observed that, as the values of θ_* decreased, new standing waves were formed downstream of the first one. The amplitude of these standing waves was reduced as they formed further downstream of the first (see figure 2). They could also become unstable, to allow a cyclone to be pinched-off from the crest of the waves. As might be expected, the pinch-off timescale for the second standing wave was considerably greater than that of the first one. We conclude that standing waves become unstable and allow a cyclone to be pinched-off when the local value of $\theta_* \leqslant 2$.

We were also interested in measuring the wavelength of the standing waves. These results are not presented here, because for those experiments with high values of θ_*, where the waves were formed far downstream of the ridge, some part of the wavetrain was not included within the field of view of the camera.

7. Summary and conclusions

We have produced a model of coastal upwelling in the laboratory and examined the effects of a combined cape and bottom topography (ridge) on the dynamics of the resultant upwelling front. We have found that a cape by itself has only a small effect. On the other hand, placing a ridge on the sloping bottom of the tank created a very strong influence on the flow both upstream and downstream of the ridge as follows.

(i) The drift velocity of the upstream waves is reduced to about 0.4 of that without the ridge.

(ii) The size of the upstream frontal waves, once well formed, remains almost constant, and their size is smaller than that of those created without the ridge in place.

(iii) When the frontal waves are approaching the ridge they deform and are finally absorbed by the jet on the ridge.

(iv) An infrequent pinch-off process of cyclones from the front occurs upstream of the ridge.

(v) The size of these pinched-off cyclones is considerably greater than that of the frontal waves, and as they drift downstream and outward they finally reach the ridge, and like the frontal waves they are also absorbed by the flow at the ridge.

(vi) The first sign of upwelling occurs as a plume on the ridge, which always migrates outward ahead of the upstream front to produce a maximum upwelling near the downstream edge of the ridge.

(vii) The presence of the ridge gives rise to a meandering jet-like motion, which starts from the upstream edge of the ridge and extends downstream in the form of a number of large-amplitude standing waves.

(viii) At higher values of θ_* the large-amplitude standing waves also have a large wavelength. The part of the jet between the maximum plume and the standing wave flows very close to the wall. At lower values of θ_* the standing wavelength is smaller, and a large anticyclone is often formed between the first standing waves and the ridge.

We have found that $\theta_* = (g'h_0)/u_* f\lambda_s$ is a suitable parameter to determine the dynamics of the coastal upwelling. For example, the front migration rate $M_f \sim \theta_*^{-1}$ and the size and drift velocity of the upstream waves are $\lambda_w/\lambda_s \sim \theta_*$ and $u_w/u_* \sim \theta_*^{0.25}$ respectively. These results indicate that Rossby deformation radius is not the only parameter determining the dynamics of the coastal upwelling.

The authors wish to thank Mr Casey De Vries for his laboratory assistance in bringing the experimental apparatus to working condition and Mrs Jacquette Givens for typing this manuscript. Financial support was from the National Science Foundation, Grant OCE-8214549.

REFERENCES

ALLEN, J. S. 1973 Upwelling and coastal jets in a continuously stratified ocean. *J. Phys. Oceanogr.* **3**, 245–257.

ARTHUR, R. S. 1965 On the calculation of vertical motion in eastern boundary currents from determinations of horizontal motion. *J. Geophys. Res.* **70**, 2799–2803.

BRINK, K. H., HALPERN, D. & SMITH, R. L. 1980 Circulation in the Peruvian upwelling system near 15° S. *J. Geophys. Res.* **85**, 4036–4048.

DOUGLAS, R. A., HIDE, R. & MASON, P. J. 1972 An investigation of the structure of baroclinic waves using three-level streak photography. *Q. J. R. Met. Soc.* **98**, 247–263.

EADY, E. T. 1949 Long waves and cyclone waves. *Tellus* **1**, 35–52.

GARVINE, R. W. 1971 A simple model of coastal upwelling dynamics. *J. Phys. Oceanogr.* **1**, 169–179.

GRIFFITHS, R. W. & LINDEN, P. F. 1981 The stability of buoyancy driven coastal currents. *Dyn. Atmos. Oceans* **5**, 281–306.

GRIFFITHS, R. W. & LINDEN, P. F. 1982 Laboratory experiments on fronts. Part 1. Density driven boundary currents. *Geophys. Astrophys. Fluid Dyn.* **19**, 159–187.

HALPERN, D. 1974 Summertime surface diurnal period winds measured over an upwelling region near the Oregon coast. *J. Geophys. Res.* **79**, 2223–2230.

HALPERN, D. 1976 Structure of a coastal upwelling event observed off Oregon during July 1973. *Deep-Sea Res.* **23**, 495–508.

HART, J. E. 1972 A laboratory study of baroclinic instability. *Geophys. Fluid Dyn.* **3**, 181–209.

HART, J. E. 1980 An experimental study of nonlinear baroclinic instability and mode selection in a large basin. *Dyn. Atmos. Oceans* **4**, 115–135.

HIDE, R. 1971 Laboratory experiments on free thermal convection in a rotating fluid subject to a horizontal temperature gradient and their relation to the theory of the global *atmospheric* circulation. In *The Global Circulation of the Atmosphere*, pp. 196–121. R. Met. Soc./Am. Met. Soc.

HULBURT, H. E. & THOMPSON, J. D. 1973 Coastal upwelling on a β-plane. *J. Phys. Oceanogr.* **3**, 16–32.

IKEDA, M. & EMERY, W. J. 1984 Satellite observation and modelling of meanders in the California current system off Oregon and Northern California. *J. Phys. Oceanogr.* **14**, 1–17.

KANTHA, L. H., PHILLIPS, O. M. & AZAD, R. S. 1977 On turbulent entrainment at a stable density interface. *J. Fluid Mech.* **79**, 753–768.

LINDEN, P. F. & VAN HEIJST, G. J. F. 1984 Two-layer spin up and frontogenesis. *J. Fluid Mech.* **143**, 69–94.

MAXWORTHY, T. 1977 Topographic effects in rapidly-rotating fluids: flow over a transverse ridge. *Z. angew. Math. Phys.* **28**, 853–864.

MOOERS, C. N. K., COLLINS, C. A. & SMITH, R. S. 1976 The dynamics structure of the frontal zone in the coastal upwelling region off Oregon. *J. Phys. Oceanogr.* **6**, 3–21.

MOOERS, C. N. K. & ROBINSON, A. R. 1984 Turbulent jets and eddies in the California current and inferred cross-shore transports. *Science* **223**, 51–53.

NARIMOUSA, S., LONG, R. R. & KITAIGORODSKII, S. A. 1986 Entrainment due to turbulent shear flow at the interface of a stably stratified fluid. *Tellus* (in press.)

NARIMOUSA, S. & MAXWORTHY, T. 1985 Coastal upwelling on a sloping bottom: the formation of plumes, jets and pinch-off cyclones. (Submitted to *J. Fluid Mech.*)

O'BRIEN, J. J. & HULBURT, H. E. 1972 A numerical model of coastal upwelling. *J. Phys. Oceanogr.* **2**, 14–26.

PEFFLEY, M. B. & O'BRIEN, J. J. 1976 A three dimensional simulation of coastal upwelling off Oregon. *J. Phys. Oceanogr.* **6**, 164–180.

PRELLER, R. & O'BRIEN, J. J. 1980 The influence of bottom topography on upwelling off Peru. *J. Phys. Oceanogr.* **10**, 1377–1398.

RIENECKER, M. M., MOOERS, C. N. K., HAGAN, D. E. & ROBINSON, A. R. 1985 A cool anomaly off Northern California: an investigation using IR imagery and *in situ* data. *J. Geophys. Res.* (to appear).

SAUNDERS, P. M. 1973 The instability of a baroclinic vortex. *J. Phys. Oceanogr.* **3**, 61–65.

YOSHIDA, K. 1967 Circulation in the eastern tropical oceans with special references to upwelling and under currents. *Japan J. Geophys.* **4**, 1–75.